HAL open science

Structural, electrical and optical properties of strontium vanadates films grown by magnetron sputtering

Axel Rouviller, Moussa Mezhoud, Alex Misiak, Meiling Zhang, Nicolas Chery, Caroline Bonafos, Ulrike Luders, Philippe Marie, Christian Dufour, Xavier Portier, et al.

▶ To cite this version:

Axel Rouviller, Moussa Mezhoud, Alex Misiak, Meiling Zhang, Nicolas Chery, et al.. Structural, electrical and optical properties of strontium vanadates films grown by magnetron sputtering. ACS Applied Electronic Materials, In press, 6 (2), pp.1318-1329. https://doi.org/10.1021/acsaelm.3c01642 . hal-04400444

HAL Id: hal-04400444

https://hal.science/hal-04400444v1

Submitted on 17 Jan 2024

HAL is a multi-disciplinary open access archive for the deposit and dissemination of scientific research documents, whether they are published or not. The documents may come from teaching and research institutions in France or abroad, or from public or private research centers.

L'archive ouverte pluridisciplinaire **HAL**, est destinée au dépôt et à la diffusion de documents scientifiques de niveau recherche, publiés ou non, émanant des établissements d'enseignement et de recherche français ou étrangers, des laboratoires publics ou privés.

Structural, Electrical and Optical Properties of Strontium Vanadates Films Grown by Magnetron Sputtering

Axel Rouviller,[*,†] Moussa Mezhoud,[‡] Alex Misiak,[‡] Meiling Zhang,[¶] Nicolas Chery,[¶] Caroline Bonafos,[¶] Ulrike Lüders,[‡] Philippe Marie,[†] Christian Dufour,[†] Xavier Portier,[†] and Fabrice Gourbilleau[†]

†*CIMAP, Normandie Université, ENSICAEN, UNICAEN, CNRS, 14050 Caen Cedex 4, France*

‡*CRISMAT, CNRS UMR6508, Normandie Université, ENSICAEN, UNICAEN, 14050 Caen Cedex 4, France*

¶*CEMES, CNRS UMR5136, 31055 Toulouse, France*

E-mail: axel.rouviller@ensicaen.fr

Abstract

$SrVO_3$ is a strongly correlated metal which has been highly studied in recent years due to its optical and electrical properties which makes it a promising transparent conducting oxide (TCO). By investigating and optimizing these interesting properties, $SrVO_3$ might be able to replace in the future Indium-Tin Oxide which is the most commonly used TCO at the current time but which suffers from resource depletion. In this study, films of about 30 nm were grown by reactive sputtering of $Sr_2V_2O_7$ target onto Si substrates, both with and without a TiO_2 buffer layer, at different temperatures, and using different ratios between H_2 and Ar during the growth. The

structural, electrical and optical properties of these films were analysed, illustrating the importance of the TiO_2 buffer layer as well as the growth parameters in obtaining conductive and transparent thin films. Moreover, the electrical and optical properties measurements revealed that these films have not actually a correlated metal behaviour but more a semi-conductor one, most probably due to a no-stoichiometry in comparison to $SrVO_3$. However, the high electrical conductivity of the obtained films are higher than one of the undoped transparent semi-conductors such as ZnO or SnO_2 currently used in the field of microelectronics. These results pave the way of using such material in devices requiring TCO properties in a Complementary Metal-Oxide-Semiconductor (CMOS) compatible approach.

Introduction

Transparent conducting oxides (TCOs) are highly sought materials for the fabrication of devices such as for example photovoltaic pannels or light-emitting diodes. Currently, the most widely used TCO material is ITO (Indium-Tin Oxide). Considering the low abundance of Indium on earth, it is important to find alternatives. In this context, perovskite $SrVO_3$ (SVO) could be a good challenger to replace ITO since its physical properties are similar.[1] This material belongs to the family of strongly correlated metals and therefore has a high effective mass. Indeed, the greater a material's electronic correlation is, the higher the effective mass m^* of the electrons. Strongly correlated metals are ideal candidates to serve as TCOs since their charge carrier density is in the same range as that of typical metals (10^{22} cm^{-1}), allowing a high electrical conductivity. Moreover, the reflection edge of the light by the free carriers, represented by the screened plasma energy, is out of the visible range due to the high m^* value, allowing a significant optical transparency in the region of interest.

Nevertheless, it has been shown that the crystallised phase of $SrVO_3$ is required to obtain the desired electrical properties since the amorphous one is electrically insulating.[2] Unfortu-

nately, the obtention of crystallised $SrVO_3$ needs the use of complex film growth methods and specific substrates such as $SrTiO_3$, $LaAlO_3$ and $(LaAlO_3)_{0,3}(Sr_2TaAlO_6)_{0,7}$ (LSAT), which makes their production hardly compatible with the standards of the microelectonic industry. In the literature, the growth of $SrVO_3$ cubic phase was carried out using molecular beam epitaxy (MBE),[1,3] pulsed laser deposition (PLD)[2,4–10] and electron-beam evaporation.[11,12] Only a few articles present the growth of $SrVO_3$ by sputtering deposition.[13,14] For all these growth approaches, the specific substrates detailed above are required to obtain the cubic phase of $SrVO_3$. Their main drawbacks is their price and low compatibility with the microelectronic standards. Thin film growth on low-cost substrates has been attempted by some groups using the sputtering method. For instance, Sharma et al have identified an orthorhombic phase in $SrVO_3$ films, which are transparent but highly resistive.[14] On the other hand, Jung et al have obtained promising results by reactively sputtering an $Sr_2V_2O_7$ target under an hydrogen rate of 25% in the plasma. They conclude that it is possible to grow $SrVO_3$ crystallized films on LSAT substrate at a temperature of 400°C. Moreover, they showed that thanks to an annealing, it is possible to obtain conductive SVO films on low cost substrates such as Si/SiO_2 and Si/TiO_2. At last, Marks et al have shown the possibility to obtain crystallized $SrVO_3$ on $SrTiO_3$ substrate by a two steps process. First of all, amorphous SVO has been deposited by RF magnetron sputtering, then, the crystallization was carried out thanks to an heating in a reducing atmosphere.[15] The growth of $SrVO_3$ on low-cost substrates using sputtering is therefore an interesting field of research to further investigate.

The main issue with film growth on low-cost substrates is the lower crystallization in comparison to monocrystalline oxide substrates that permit an epitaxial growth. Recent works have shown that the presence of a TiO_2 film between the substrate and the film favors in-situ cubic crystallization of $SrVO_3$.[16,17]

In this work, we report experimental investigations on the growth of transparent and conductive films by sputtering of $Sr_2V_2O_7$ target on Si substrates both with and without a TiO_2 seed layer. During this study, the obtained films have not been annealed. We investigated the influence of the substrate temperature T_G and the hydrogen rate r_H on the structural, electrical and optical properties of the resulting films without any post annealing process. The aim of this study was to find suitable sputtering parameters in order to obtain optimal physical properties for specific functionalities in the microelectronic and optoelectronic industries.

Experimental details

The silicon substrates used in this study were single crystalline, (100) oriented and p-doped with a resistivity in the 5-15 Ω.cm range. Some of the Si substrates were coated with about 38 nm-thick of anatase TiO_2 (tetragonal structure with a = 3.79 Å and c = 9.51 Å) by atomic layer deposition (ALD). More details on this growth can be found elsewhere.[18] On these two types of substrates, thin films of $SrVO_3$ were grown by reactively sputtering 2" target of $Sr_2V_2O_7$ in a hydrogen rich plasma. The introduction of hydrogen allows to reduce the oxygen species in the plasma and therefore to control the oxygen incorporation in the layer as previously demonstrated in Si/SiO_2 multilayers.[19,20] For this study, the radio frequency sputtering power applied on the target was 45 W and the plasma pressure was set at 3 mTorr for all deposits. Three series of samples were prepared. For the first series, the hydrogen rate r_H in the plasma was set to 50% while the substrate temperature T_G was varied from 400°C to 550°C with a 50°C step in order to study the influence of this parameter on the film properties. For the second series, T_G was fixed at 500°C and the hydrogen rate r_H varying from 0 to 80%. Finally, the third series was the same as the second one, but with a T_G fixed at 550°C. These two last series aim at studying the influence of hydrogen incorporation in the plasma on film characteristics.

The structural properties of the films were studied using grazing incidence X-ray diffraction (GIXRD). The diffractometer used was a D8 Bruker Discover, equipped with a Cu source ($\lambda_{k_{\alpha 1}} = 1,5406$Å). Nanoscale observations and crystallographic analyses were made by transmission electron microscopy (TEM) (Cold FEG double corrected JEOL ARM200 operated at 200 kV) using the DigitalMicrograph software by GATAN for the image processing. Chemical maps were performed owing to STEM EDX data. The EDX spectrometer was a CENTURIO equipment from JEOL. For TEM observations, the thin films were prepared by focused ion beam (FIB) (Dual beam FEI Helios nanolab 660) method such that cross sectional observations of the films were following a [110] direction of the Si substrate were possible. The surface topographies of our films were investigated by atomic force microscopy (AFM) in tapping mode using a Nanoscope III device from Digital Instruments. The AFM images were corrected for flatness using the Nanoscope software and the RMS roughness was estimated from AFM digitized images with a scan area of 4 μm^2.

The resistivity at room temperature was measured by the four probe method with a keithley 2450 sourcemeter. Moreover, the resistivities of the most interesting samples were measured from 5 to 300 K using the Van der Pauw configuration with a physical properties measurement system (PPMS) by Quantum Design. Hall measurements were carried out to determine the carrier concentration and their mobility using a magnetic field which varied from -9 to +9 Tesla. It is important to note that all the samples used for electrical experiments were grown on substrates containing an additional 8 μm thick thermal SiO_2 layer between the Si substrate and the top layer in order to eliminate the contribution of the conductivity of the substrate during measurements.

At last, optical measurements were carried out by using spectroscopic ellipsometry with an incident light energy which varied from 1.5 to 6 eV and under incident angles of 65, 70, and

75° with respect to the normal incidence (UVISEL 2 Jobin-Yvon). Once the measurements acquired, the software DeltaPsi2 allowed us to simulate the data and obtain the thickness and optical properties of the films.

Results and discussion

Structural properties

Figure 1 displays the GIXRD patterns of as grown SVO films resulting from the sputtering of $Sr_2V_2O_7$ target onto (100) Si substrates with and without a TiO_2 buffer layer. Figure 1a shows the GIXRD patterns of SVO films grown at a substrate temperature T_G of 500°C and with a hydrogen rate r_H of 50%, on both substrates. For the sample without TiO_2, no diffraction peak can be observed in the range of 30 to 50°, whereas three peaks characteristics of crystallized $SrVO_3$ can be observed when TiO_2 anatase is present. This demonstrates that the TiO_2 buffer layer favors in-situ crystallization of $SrVO_3$. The use of a TiO_2 buffer layer seems to be essential in order to obtain crystallized SVO layers on low-cost substrate without annealing. This better in-situ crystallization is explained by the weak mismatch between the two materials.[16] This demonstrates that the TiO_2 buffer layer favors in-situ crystallization of $SrVO_3$. Figure 1b highlights the increasing crystallization of the films thanks to the rise of T_G. From T_G = 450°C, peaks around 32.6° and then for higher temperature also around 46.1°, which correspond to the (110) and (200) lattice planes of cubic $SrVO_3$, respectively, can be observed, whereas they are not present for T_G = 400°C. This result emphasizes the importance of the growth temperature for the achievement of crystallised cubic $SrVO_3$. However it should be noted that the angles obtained are slightly lower than those expected. Indeed, in the literature, these peaks are found at 33.0° and 47.3°, respectively. This shift to lower angles could be explained by the stress exerted by the anatase TiO_2 buffer layer on the lattice of the $SrVO_3$ film. Indeed, anatase TiO_2 has a lattice parameter of 3.79 Å whereas that of bulk cubic $SrVO_3$ is 3.84 Å leading to a mismatch of -1.33%. Thus such a buffer

layer creates compressive stress on the growing film which results in greater out-of-plane lattice parameters for the $SrVO_3$ thin films. Another explanation for this behaviour on the GIXRD pattern, for SVO films, could be a non-perfect stoichiometry, which can also lead to larger lattice parameters as repoted in literature.[3,4] The increase of T_G also causes the appearance of a peak around 42.2° and of another large peak with a lower intensity around 38.1°. These peaks are characteristic of the $Sr_3V_2O_8$ phase. Note that $Sr_3V_2O_8$ has also a peak at 40.5°, which corresponds to the $SrVO_3$ (111). Figure 1c presents the influence of r_H on the crystallization of the films for T_G = 500°C. We note that no peaks corresponding to crystallized $SrVO_3$ and $Sr_3V_2O_8$ are detected under a value of r_H of 50%. Such a result indicates that if there is not enough H_2 during the growth, the amount of oxygen originating from $Sr_2V_2O_7$ will be too high to allow the formation of crystallized phase of $SrVO_3$. This is confirmed by the XRD spectra achieved with higher hydrogen rate ranging from 50% to 80% and reported in Figure 1d in which one can observe the characteristic peaks of $SrVO_3$ and $Sr_3V_2O_8$ for all three films.

Most of the GIXRD patterns present a peak around 48.1° that corresponds to the anatase TiO_2 (200) crystallographic plane and whose intensity decreases with the increase of T_G and / or r_H. This evolution with the deposition parameters could be explained by two coupled effects. The first one is an etching process due to the presence of H-species in the plasma which reduces the volume of the crystalline buffer layer. The other one is the crystallization of the SVO layer, which results in a higher density and therefore reduces the penetration of the X-rays in the film.

To complete our data on the structural properties of the films, TEM observations were carried out. Figure 2 shows an HRTEM image of a 35 nm thick SVO film grown at 500°C, with a hydrogen rate r_H of 50%, on a (100) silicon substrate. Most of the film is amorphous which confirms the results provided by XRD. However, some small regions in the upper part

of the film are found to be crystalline with the presence of nanocrystalline grains about 10 nm wide as attested by the enlarged region. The corresponding Fast Fourier Transform (FFT) is consistent with a [010] projection of the $SrVO_3$ cubic structure (a = 3.84 Å). The low fraction of the crystalline material in the film explains the lack of $SrVO_3$ characteristic peaks in the XRD pattern of 1a. But this is a promising result that shows that under very specific parameters to be carefully defined, it could be possible to grow crystalline $SrVO_3$ film without the use of a crystallized buffer layer. However, in the following, only the experimental results for the films grown with a TiO_2 buffer layer are presented.

Figure 3 is a summary of TEM results obtained from a TiO_2/SVO structure grown on (100) Si, at 550°C and r_H = 60%. Figure 3a is a typical bright field TEM image showing the whole structure with the stacked layers. The thicknesses are about 28 nm for TiO_2 and $SrVO_3$ sublayers. This observation evidences that the TiO_2 sublayer has been submitted to the etching by the hydrogen species of the plasma since its original thinckness was estimated to be about 38 nm by ellipsometry measurements. Such process is well known and has been evidenced in Si/SiO_2 system by Ternon et al.[20] These authors have shown that the presence of hydrogen in the plasma favors an etching phenomena of the growing layer which is dependent on the level of the hydrogen rate in the plasma. We observe, in the same way as these authors, a decrease of the average deposition rate as the function of the hydrogen rate for growing layer. Note that in some part of the sample, the TiO_2 layer thickness has lost about 20 nm due probably to a selective crystallographic etching by the hydrogen species (not shown here). One can also notice the native thin SiO_2 layer (2-3 nm) between the Si substrate and the buffer layer. Figures 3(b) and 3(c) are HRTEM images of enlarged regions of TiO_2 and $SrVO_3$, respectively. The FFT pattern in the inset of Figure 3c is in agreement with the cubic structure of $SrVO_3$ along the [010] direction. At last, Figure 3d depicts Ti, Sr and V chemical maps of the whole structure. Interestingly, the V map clearly shows a contrast in the TiO_2 sublayer. This reveals a V diffusion from the SVO film toward the TiO_2

layer, which can also contribute to the loss of crystallinity of the TiO_2 layer evidenced on the XRD spectra (Figure 1). The V concentration detected in the TiO_2 layer is less than 1%. The same interdiffusion has been also observed for a growth of $SrVO_3$ on TiO_2 using PLD.[17]

In order to study the effect of the hydrogen rate on the films, the surface roughness was investigated by AFM (Figure 4). These 3D images clearly show that the films grown with r_H = 20% (Figure 4a) and r_H = 50% (Figure 4b) at T_G = 500°C present a homogeneous roughness over the entire surface of the films. For T_G = 500°C and r_H = 80% (Figure 4c) or T_G = 550°C and r_H = 50% (Figure 4d), the AFM scanning reveals the presence of several irregularly distributed bigger domains over the entire surface of the films. Figures 5a and 5b show the average roughness obtained by AFM measurements, with images of 2.5 μm x 2.5 μm images, and the corresponding value deduced from ellipsometric modeling as a function of T_G for r_H = 50% and as a function of r_H for a substrate temperature T_G of 550°C. At first glance, one can notice the consistency of the evolution between the two curves of Figure 5a showing an increase of the roughness with the growth temperature. This result highlights that the higher the deposition temperature is, the greater the etching of the film. For T_G = 550°C, we observe a slight evolution of the roughness up to r_H = 70% followed by an important increase between r_H = 70% and r_H = 80% (Figure 5b). This trend is also oberved for a growth temperature value of 500°C. Here again, the evolutions of the roughnesses deduced from either AFM or ellipsometric measurements are similar demonstrating that the model carried out thanks to the ellipsometriy measurements is accurate. These investigations reveal that if a high hydrogen rate in the plasma is necessary to achieve an in-situ crystallization of the films, it is also leads to an important surface roughness of them and therefore may have consequences on their physical properties. Indeed, concerning the electrical properties, the diffuse scattering of conduction electrons of a rough surface results in an increase of the electrical resistivities of the films.[21–23]

Electrical properties of the films grown with a TiO_2 buffer layer

The resistivity values at room temperature obtained by the 4 probe method are reported in Figure 6. Figure 6a displays the evolution of the resistivity as a function of the growth temperature for $r_H = 50\%$. We can see that the resistivity is high and constant until 450°C before decreasing significantly when the deposition temperature reaches 500°C. The high resistivity value achieved for the lowest deposition temperature (about 23×10^{-3} Ω.cm) is attributed to the mainly amorphous nature of the film whereas its decrease to 7.5×10^{-3} Ω.cm is correlated with the appearance of diffraction peaks characteristic of cubic $SrVO_3$ (Figure 1b). By increasing the deposition temperature by 50°C, the resistivity achieved the value of about 3×10^{-3} Ω.cm for an hydrogen rate in the plasma of 50%. This evolution of the electrical properties can therefore be explained by the crystallization of the deposited films with the growth temperature. For a given growth temperature, the same trend can be observed with the increased hydrogen rate (Figure 6b). Without hydrogen during the deposition, the resulting layer is amorphous and has the characteristics of an insulating layer as expected with a resistivity as high as 550 Ω.cm. But a rate of 20% of H_2 in the plasma allows to improve this value by 4 orders of magnitude to reach 5.2×10^{-3} Ω.cm, demonstrating the reactive effect in the reduction of the sputtering of the $Sr_2V_2O_7$ insulating target. By continuously increasing the hydrogen rate in the plasma, we observe an improvement of the resistivity of the lowest resistivity around 1.1×10^{-3} Ω.cm for $r_H = 80\%$ at 550°C. This is to our knowledge the best resistivity value ever reported in the litterature for such a $SrVO_3$ layer deposited by sputtering on a low cost substrate and in a large scale approach.[13] Nevertheless, this value remains higher than the resistivities of monocrystalline $SrVO_3$ films grown on LSAT, due to the polycristalline nature and the non-optimal crystallization template of the films. To confirm the essential role of the TiO_2 buffer layer, 4 probes measurements have been performed on the layer grown directly on the Si substrate at $T_G = 500$°C and with $r_H =$

50%. The resistivity achived for this layer is $\rho = 226.5$ Ω.cm, whereas the same layer grown on the same substrate but with TiO_2 buffer layer presents a resistivity value of 9.2×10^{-3} Ω.cm. This confirms again the essential role played by the TiO_2 buffer layer in the in-situ crystallization process of the $SrVO_3$ films and consequently on its physical properties.

The evolutions of the resistivities of the different samples as a function of temperature are presented in Figure 7 : Figure 7a for different T_G at a hydrogen rate r_H of 50% and in Figure 7b for different r_H% values at a fixed T_G of 550°C. These evolutions are not corresponding to a cubic $SrVO_3$ material which is supposed to have a metallic behaviour with its resistivity increasing with temperature.[4,7,24] Indeed, Figures 7a and 7b clearly show the resistivities of the films decreasing with the increasing temperature. In contrast to theoretical analyses based on density functional theory, which showed that cubic $SrVO_3$ can only, by nature, be metallic, such behaviour is typical of a semiconductor material.[25] Considering that $Sr_2V_2O_7$ is an insulating material and $SrVO_3$ is a conductive one, we can hypothesize that the films obtained are over-oxidized $SrVO_3$ or under-oxidized $Sr_2V_2O_7$. This means the stoichiometry of these films might actually be $SrVO_{3+x}$ with x comprised between 0 and 0.5, which could confirm the interpretation for the shift of the characteristic peaks of $SrVO_3$ on GIXRD pattern. Another explanation might be the presence of the $Sr_3V_2O_8$ phase observed by GIXRD, which could modify the electrical properties of the films. In the Rath et al paper, SVO films grown by PLD on glass/TiO_2 showed a metallic behavior.[17] This means that the semiconducting behavior observed here is not caused by the TiO_2 buffer layer but by the specific conditions of the sputtering growth process. Note that to our knowledge, no data have been reported on the physical properties of such a material grown with this process in the literature. The films grown with optimized values of r_H and T_G in this study are more conductive than undoped thin films of semiconductors used as TCOs, such as ZnO[26–28] and SnO_2[29–31] with resistivity values of 4.3×10^{-3} Ω.cm and 4.5×10^{-3} Ω.cm, respectively. The obtained layers are also more conductive than thin films of Al doped ZnO before annealing for which the

electrical resistivity is around 3.3×10^{-3} Ω.cm.[32–34] Consequently, our vanadate films with a resistivity between 1 and 2×10^{-3} Ω.cm offer potential applications in the microelectronics field since our approach is fully compatible with the standard of the microelectronic industry.

In Figure 8, the charge carriers charateristics at room temperature as a function of the growth parameters are presented. Figure 8a displays the evolution of the carrier concentration (orange) and the carrier mobility (purple) as a function of the growth temperature for a hydrogen rate of 50%. We can observe a spectacular increase of the carrier concentration as a function of T_G. Indeed, the carrier concentration is around $5 \times 10^{19} cm^{-3}$ for T_G = 400°C and it increases by approximately 2 orders of magnitude for T_G = 550°C. We can also notice a decrease of the carrier mobility with T_G with a mobility 6 times lower at 550°C than at 400°C. These evolutions are explained by the crystallization of the layers, as evidenced on the GIXRD patterns (Figure 1b). The crystallization of SVO leads to the correlated conduction regime characterized by high charge densities and low mobilities related to the high effective mass. In Figure 8b, the evolutions of the carrier concentration and of the mobility with r_H from 50 to 80%, for a given growth temperature of 550°C, are shown. We can note an increase of the carrier concentration in this range until a maximum value is reached around $1.45 \times 10^{22} cm^{-3}$. This value is consistent, but slighly lower, when compared to the values found in the literature for cubic $SrVO_3$ grown on monocrystalline substrates.[1,4,6,13] This result demonstrates the importance of the hydrogen rate level to reach a carrier concentration value characteristic of crystallized $SrVO_3$. The fact that the carrier concentration is low under non-optimal growth conditions underlines that the oxygen-stoichiometry is likely too high. This leads to an overoxidation to the V^{5+} state, and therefore low charge concentrations. In terms of carrier mobility, we note a decrease between the r_H values of 50 and 60% and after 60% an almost constant value of approximately 0.47 $cm^2.V^{-1}.s^{-1}$.The films obtained in this study are polycristalline which entails carrier scattering by the grain boundaries and limits their mobility. This explains why our obtained values are lower than

those found in the literature for monocristalline $SrVO_3$ thin films, situated between 1 and 2 $cm^2.V^{-1}.s^{-1}$.[1,4,6,13] Another reason is that our layers are rougher than those of literature. Therefore, as explained earlier, the charge carriers of our films can also be diffused by their rough surfaces. However, with the data presented in this article we cannot conclude on the predominance of one of the two phenomena.

Based on these findings, the evolution of the carrier mobility as a function of the measurement temperature has been investigated for layers deposited at 550°C with a 60 and 70% hydrogen rate Figure 9a. The evolution unveils the existence of a low and of a high temperature regime between 50 and 300 K with an increase of the mobility between 50 and 200 K followed by its decrease between 200 and 300 K. In the literature, theoretical investigations have been reported aiming at understanding the electron scattering by ionized impurities in semiconductors.[35,36] They have shown that, at low temperature, the mobility follows a $T^{3/2}$ law due to the charge carrier diffusion. Whereas, other articles have reported that, the mobility follows a $T^{-3/2}$ law in the high temperature regime caused by the diffusion of the carriers by the acoustic phonons.[37–39] In Figure 9a, dashed lines following $T^{3/2}$ and $T^{-3/2}$ are provided as a guide to the eye, in the low and high temperature ranges, to evidence the good agreement between our measurements and the theoretical predictions, which confirms the semiconductor behaviour of the films. Concerning the evolution of the charge carrier concentration with temperature, a high and a low temperature regime is also observed (Figure 9b). For the low temperature regime we note an atypical decrease of the carrier concentration as a function of the temperature as already observed for several different semiconductors such as GaAs, In_2O_3, In_2O_3-ZnO and Mg_3Sb_2, and attributed either to the presence of impurities or vacancies.[40–43] We can hypothesize that a similar mechanism occurs in our films which explains the observed decrease of carrier concentration with the measurement temperature. By contrast, the charge carrier concentration increases as a function of the temperature in the high temperature regime. Therefore, it appears that the amount of charge carriers in

the conduction band increases thanks to their increased thermal energy. It is possible to show that, when charge carriers pass from a donor level towards the conduction band, the evolution of the conductivity (σ) as a function of the temperature follows[44] :

$$ln(\sigma) = ln(A) - \frac{\Delta E_a}{2k_B T} \tag{1}$$

Where A is a constant, ΔE_a an activation energy and k_B the Boltzmann constant. Figure 9c presents the evolution of the plot of ln(σ) as a function of $\frac{1000}{T}$, in the high temperature regime, for samples grown at 550°C with a hydrogen rate of 60 and 70%. We can observe that, for these two samples, the linear adjustments using the equation 2 fit well the experimental data well, which confirms our hypothesis about the increase of the number of charge carriers in the conduction band at high temperatures. Activation energies of approximately 18.7 meV and 12.5 meV were obtained for the samples grown with r_H = 60% and r_H = 70% respectively. However, another model is currently used to describe carrier transport in disordered semiconductors. This model is called Mott's variable range hopping (MVRH) and in this model, the electrical conductivity evolves according to the temperature as[45–48] :

$$ln(\sigma) = ln(B) - \left(\frac{T_m}{T}\right)^{1/4} \tag{2}$$

Where B is a constant and T_m the Mott temperature. Figure 9d presents the evolution of the plot of $ln(\sigma)$ as the function of $\left(\frac{1000}{T}\right)^{1/4}$, in the high temperature regime, for exactly the same samples as those of Figure 9c. We can observe that, here again, the linear adjustments fit the experiment data well. Considering that these two models fit the experiment data with $R^2 = 0.999$ for the two samples, we cannot conclude about the conductivity mechanism which takes place in the obtained layers with the data presented in this article.

Optical properties of the films grown with a TiO_2 buffer layer

The electrical characteristics of the films have been detailed in the previous part, and in order to complete the study of their TCO properties, we will now study their optical properties. Figure 10 presents the evolution of the refractive index at 1.95 eV as a function of the hydrogen rate for a given growth temperature of 550°C. In this figure, we can observe that, without hydrogen during the deposition, the resulting $SrVO_3$ layer has an optical index of 2.06, decreasing as a function of r_H until it reaches a value of 1.85 for the film grown with 80% of hydrogen. Theoretical analyses based on density functional theory have shown that the optical index at 1.95 eV of $Sr_2V_2O_7$ is around 2.10,[49] and Roth et al in their study on the growth of cubic $SrVO_3$ by MBE on LSAT substrates have reported a value of 1.75.[50] Therefore, Figure 10 highlights again the importance of the amount of hydrogen in order to reduce the oxygen of the $Sr_2V_2O_7$ target during the growth process. This result is consistent with the electrical measurements since, as demonstrated earlier, the layer deposited without hydrogen is insulating while the one grown with 80% of hydrogen has a carrier concentration close to the values presented in the literature for $SrVO_3$.

The real and imaginary parts of the dielectric permittivity ($\epsilon = \epsilon_1 - i\epsilon_2$) were extracted from the spectroscopic ellipsometry data. Figures 11a and 11b present, respectively, the evolution of ϵ_1 and ϵ_2 in the range of 0.6 to 6.5 eV for different r_H values and a growth temperature of 550°C. These two figures show the presence of peaks for ϵ_1 and ϵ_2 and we can observe that a shift of these peaks takes place for a r_H value between 50 and 60%. Indeed, ϵ_1 reaches a maximum at 4.20 eV for the layer grown with a hydrogen rate of 50% whereas, for the other films deposited with higher r_H, this maximum is achieved for 3.80 eV. For ϵ_2, the peak is shifted from 4.80 to 4.50 eV. However, the shape of the permittivity curves for the obtained films does not match with those reported in the literature.[1,6,7,51] Indeed, contrary to what we observe, ϵ_1 is usually negative for energies between 0.6 and 1.3 eV and is supposed to go through 0 before reaching a maximum at a value of 3.10 eV, while ϵ_2 should present

a maximum around 3.30 eV. Mirjolet et al explained that for $SrVO_3$, the screened plasma energy $E_{\omega_p^*}$ can be determined thanks to the relation $\epsilon_1(E_{\omega_p^*}) = 0$.[8] However, this approach only works when SVO is a strongly correlated metal for which the Drude model accurately describes the contribution of the free electrons to the permitivity at low energy, but does not work for semiconductors since ϵ_1 does not go through 0. In conclusion, in agreement with the electrical measurements, the permittivity spectra confirm that our films lack the properties of strongly correlated metals.

In order to study the optical absorption of the light by our samples, Tauc plots were depicted by plotting $(\alpha h\nu)^x$ as the function of $h\nu$ where α is the absorption coefficient (extracted from the ellipsometric models) and $h\nu$ the incident photon energy (Figure 12a). For a direct optical transition, x is equal to 2 whereas it is equal to $\frac{1}{2}$ in the case of an indirect transition.[52,53] We have therefore plotted two graphs for the layer grown with a hydrogen rate of 50% at 550°C in Figure 12a. The dashed orange curve represents the case of an indirect optical transition and the dashed purple curve represents the case of a direct optical transition. These two curves present linear parts and we can consequently determine the energy bandgap for a direct and an indirect absorption (orange and purple lines). Bandgap values between 4.11 eV and 3.80 eV were obtained for direct transitions. However, considering that the visible range is between 1.55 and 3.25 eV, this direct transition will not have any impact on the TCO properties of our films. The evolution of the energy bandgap for an indirect transition as a function of r_H, for a given growth temperature of 550°C, is shown in Figure 12b. A decrease of this indirect bandgap as a function of the hydrogen rate can be noted. Indeed, for a r_H of 50% this energy is equal to 2.97 eV while we obtained a value of around 2.72 eV for a r_H of 80%. In literature, a value of 2.70 eV is found for the indirect transition of $SrVO_3$ and is associated to an excitation of an electron from the oxygen 2p band to the empty V 3d-t_{2g} band.[8,54] We can therefore conclude once again that, the higher the hydrogen rate is during the growth process, the more the resulting layer has physical

properties which tend towards those of $SrVO_3$.

To determine the optical transparency of our films, we used the following formula :

$$T = (1 - R - d\alpha) \times 100 \tag{3}$$

Where d and α are respectively the thickness layer and the absorption coefficient extracted from the model obtained thanks to the ellipsometry measurements. The value of the reflectivity (R) for a perpendicular light incidence has been calculated using the relation :

$$R = \left(\frac{N_2 - N_1}{N_2 + N_1} \right)^2 \tag{4}$$

Where N_2 is the optical index of the vanadate layer, also extracted from the ellipsometric model, and N_1 is the optical index of air ($N_1 = 1$). Figure 13a presents the evolution of the optical transparency for different values of T_G with $r_H = 50\%$. We note a sharp increase of the optical transparency in the visible range starting from 500°C. This increase of the optical transmittance in the visible range is concomitant with the emergence of the peaks characteristic of cubic $SrVO_3$ in the GIXRD patterns (Figure 1b). The growth temperature is therefore a key parameter in order to improve the optical transparency of the samples in the visible range, thanks to the improved crystallization of the films. Figure 13b presents the evolution of the transmittance for different values of r_H with a growth temperature of 550°C. The layer formed without hydrogen is the sample with the best transparency, and as r_H increases, we see a drop in transmittance. Stated differently, the optical transmittance decreases with increasing electrical conductivity of the resulting layer (Figure 6b). Using Hall measurements, we have demonstrated that the carrier concentration increases with the hydrogen rate (Figure 8b). Futhermore, as shown by the Tauc plots (Figure 12b), films produced with a high hydrogen content exhibit an indirect bandgap transition in the visible

region. Thus, the decrease of the transmittance can be explained physically by the fact that the visible light can be absorbed and reflected by a layer's charge carriers to a greater extent as it grows with a significant amount of hydrogen. Gu et al. had previously noted in their literature the difference in optical transparency between the conductive and insulating vanadates layers.[55] These two physical behaviours can therefore explain the decrease of the transmittance as a function of r_H. We note that the obtained films are less transparent than thin films of semiconductors used as TCOs, such as ZnO and SnO_2 which present optical transmittance of about 85% in the visible range.[26,31] However, even the layer grown with a hydrogen rate of 80% has a minimum transparency higher than the maximum transparency of some SVO films reported in the literature (63%),[1,10] which were grown by PLD and have a thickness of around 45 nm.

Conclusion

In conclusion, the growth of vanadate films on Si both with and without a TiO_2 seed layer by magnetron sputtering using sputtering of a $Sr_2V_2O_7$ target was carried out successfully. Their structural, electrical and optical properties were examined. The first conclusion that could be drawn from these measurements is that the TiO_2 seed layer is necessary to obtain a fully crystallised SVO film with TCO physical properties. Secondly, even with the seed layer, T_G and r_H are both crucial growth parameters to consider in order to optimize the electrical and optical properties of the obtained films. These properties were optimized for a growth temperature of 550°C and an important amount of hydrogen in order to have a conductive film. Thirdly, the optical properties of SVO films grown on low cost substrates by magnetron sputtering were presented, which complements the existing literature. Finally, with these optimized growth parameters, the vanadate films are semiconductors which possess a higher electrical conductivity than those of the semiconductors currently used as TCOs and with optical transparency higher than 63% in all the visible range.

Several options can be considered to further improve the physical properties of these films. Heat treatments after deposition could be attempted to favor the formation of the crystalline phase and then to enhance the optical and electrical properties. In-situ annealing under vaccum or a reducing atmosphere could also be carried out in order to avoid the oxidation of the films (and the appearance of $Sr_2V_2O_7$) and a potential decrease of the electrical conductivity. Furthermore, a passivation of the films under H_2 could heal damaged atomic bonds and thus increase the electrical conductivity, as it is the case with Si-based microelectronic devices. At last, the doping of these films with luminescent ions could also be attempted in order to obtain luminescent materials for optoelectronic functionalities.

A study by sputtering of an $SrVO_3$ target could be also interesting in order to reduce the H_2 amount in the plasma during the growth and obtain less rough films.

Acknowledgement

This research was partly funded by l'Agence Nationale de la Recherche (ANR) through the LEDVAN project "ANR-23-CE50-0005-01". This work was also supported by the CNRS Federation IRMA - FR 3095 and the Normandy Region through the BOSEED project. Xavier Portier thanks the ANR (Agence Nationale de la Recherche) institution and the Normandy Region for their financial support in acquiring the FIB setup (ANR-11-EQPX-0020).

The authors thank Cédric Frilay for the preparations of the TiO_2 seed layer by ALD and Franck Lemarié to the AFM mesurements and the FIB preparations.

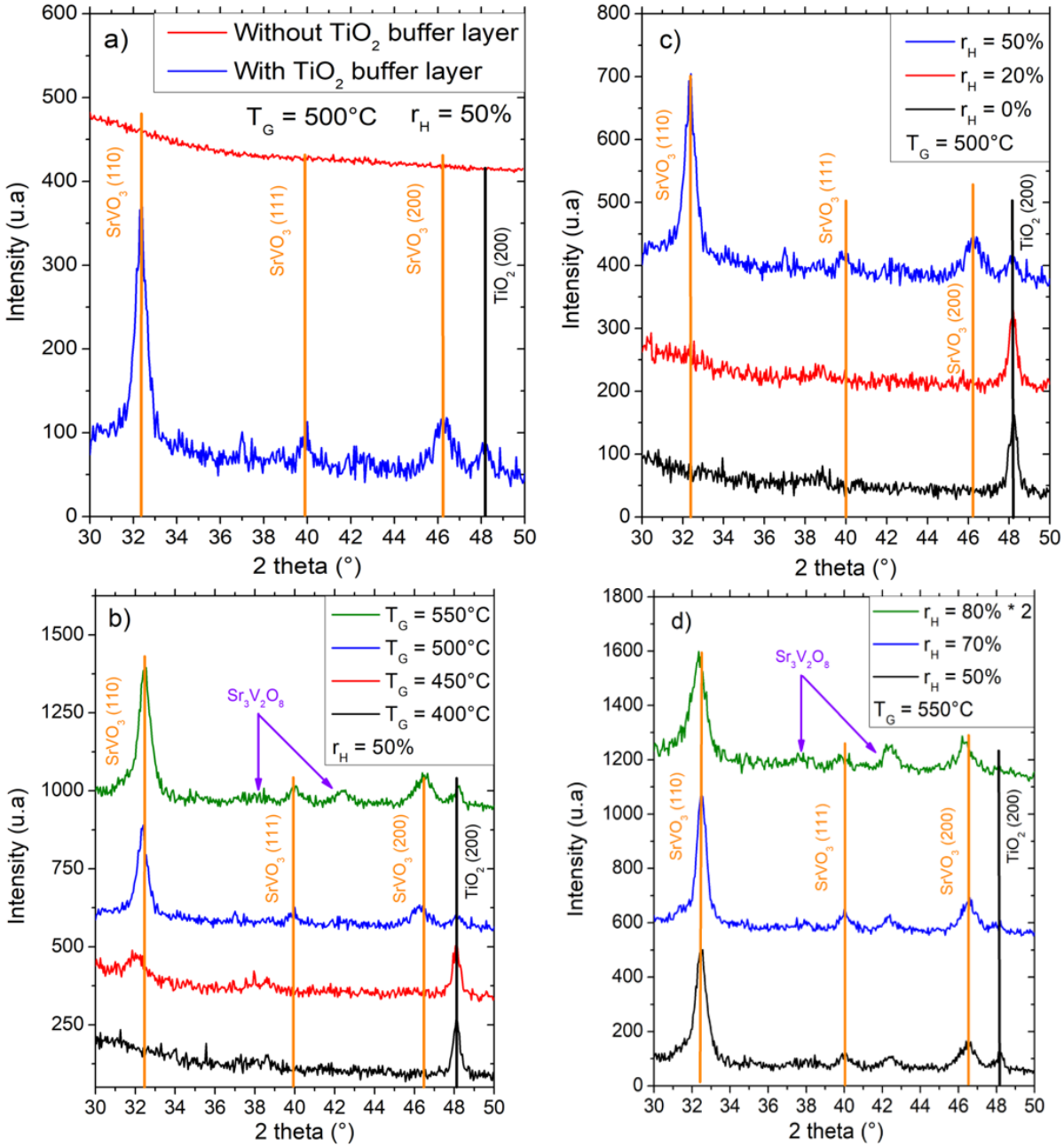

Figure 1: GIXRD patterns of thin film grown with sputtering of $Sr_2V_2O_7$ target a) with and without a TiO_2 seed layer b) for different values T_G and $r_H = 50\%$, c) for different values of r_H and $T_G = 500°C$, d) for different values of r_H and $T_G = 550°C$.

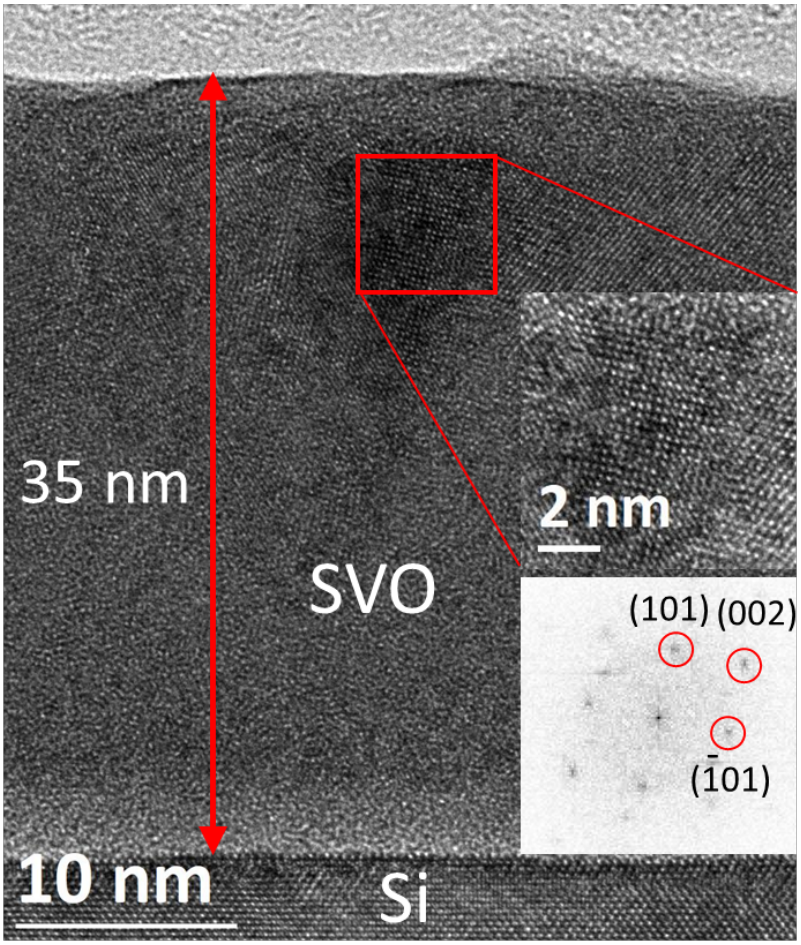

Figure 2: Typical HRTEM image of a $SrVO_3$ film grown directly on a (100) Si substrate, at 500°C with $r_H = 50\%$. $SrVO_3$ small grains are cleary visible in the film.

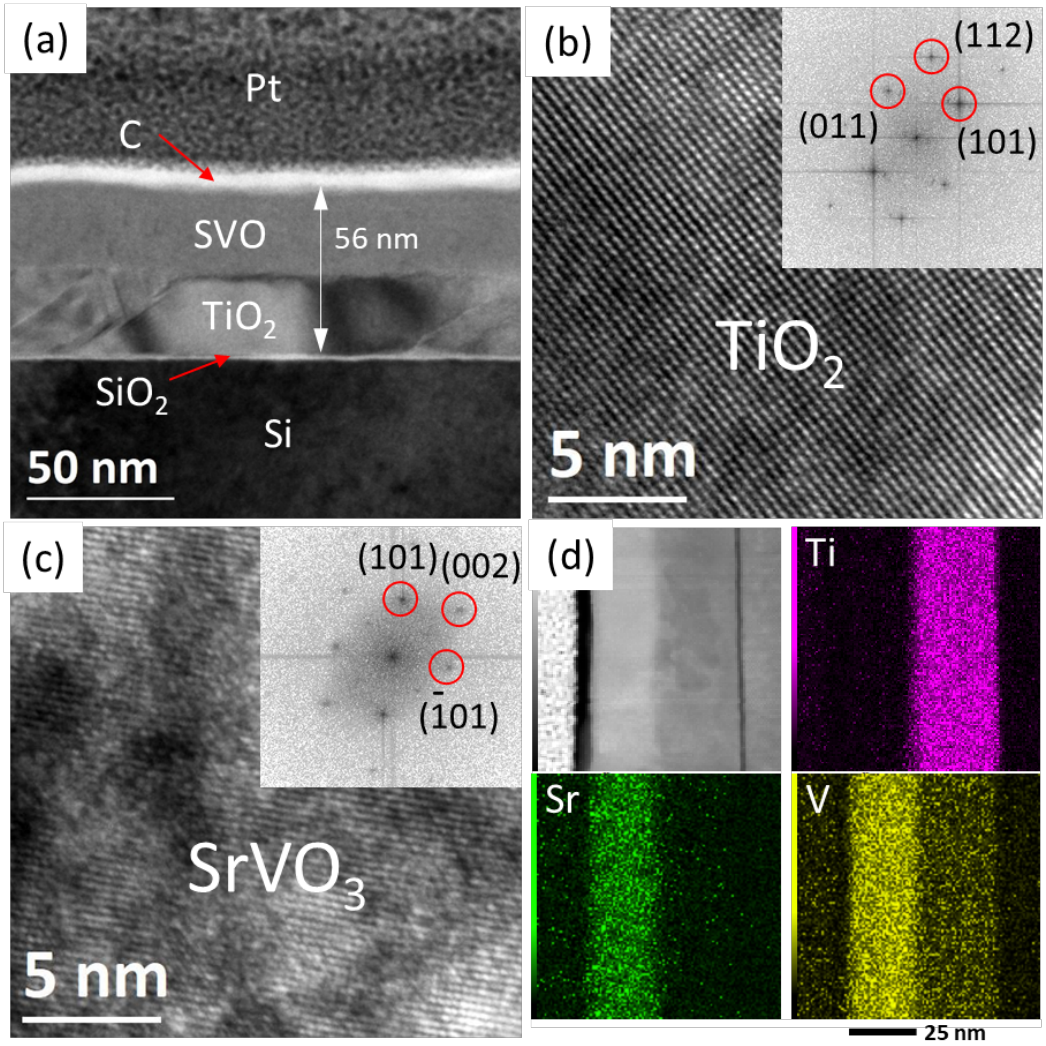

Figure 3: (a) Bright field TEM image of a TiO_2/SVO film grown on (100) Si. TiO_2 was grown by ALD and SVO by sputtering at 550°C and using $r_H = 60\%$. (b) HRTEM image of a TiO_2 region. The FFT in inset is consistent with the anatase structure projected along the [-1-11] direction. (c) HRTEM image of a SVO region with the corresponding FFT in inset. This latter is in agreement with a [010] direction of $SrVO_3$. (d) STEM HAADF image and the corresponding STEM EDX chemical maps of Ti, Sr and V.

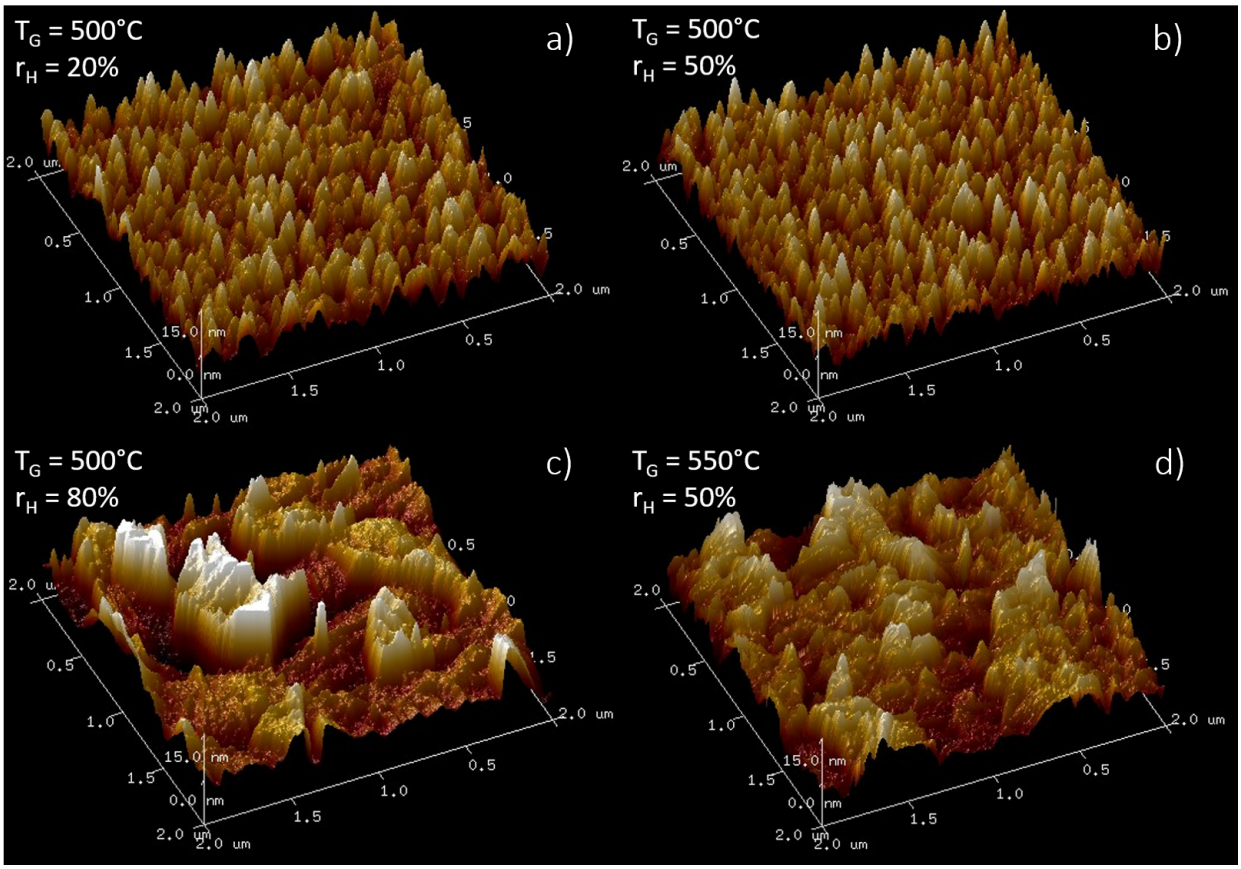

Figure 4: AFM images of the films obtained by sputtering of $Sr_2V_2O_7$ target on Si substrates and anatase TiO_2 seed layer. a) for T_G = 500°C and r_H = 20%, b) for T_G = 500°C and r_H = 50%, c) for T_G = 500°C and r_H = 80%, d) for T_G = 550°C and r_H = 50%. AFM images are 2 μm x 2 μm

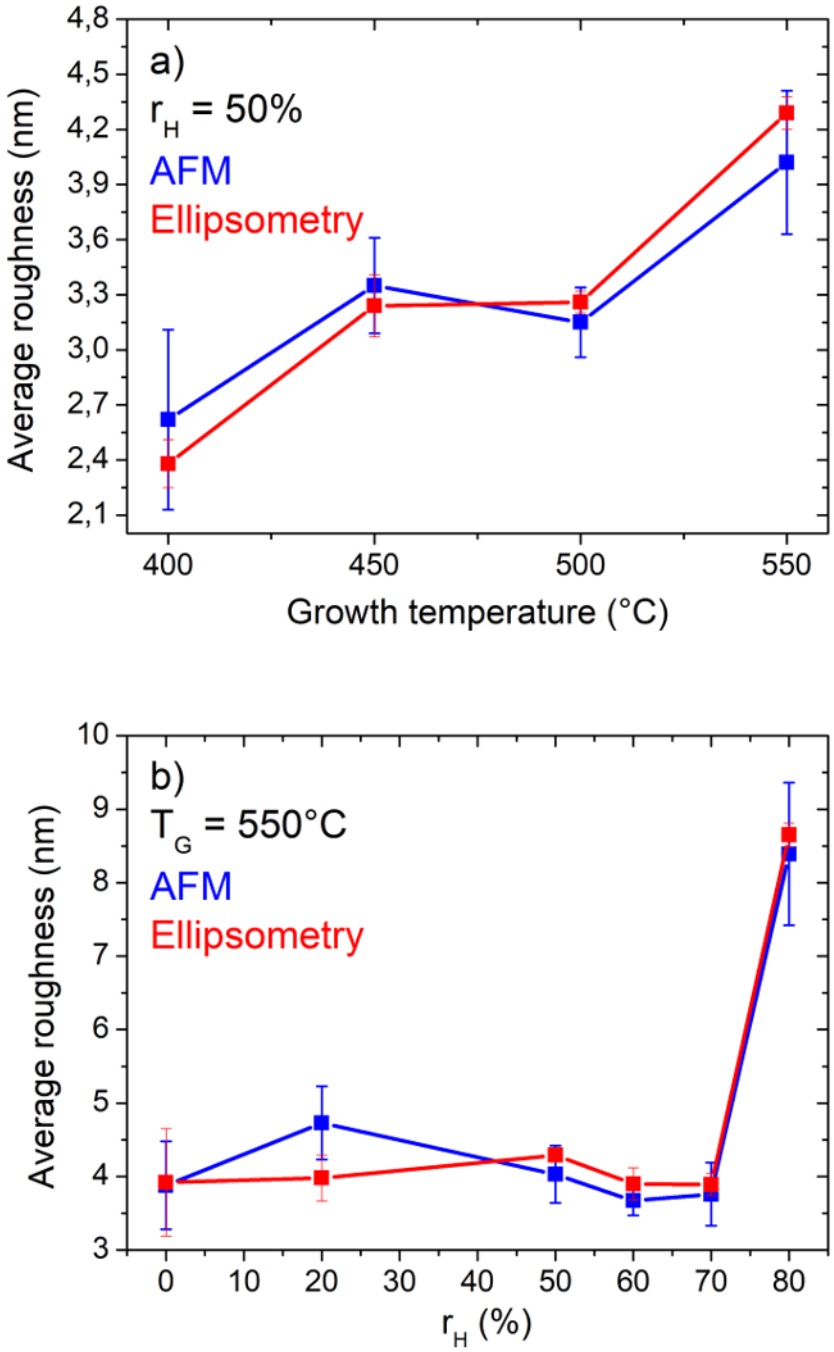

Figure 5: Evolution of the RMS roughness and the roughness derived from ellipsometric model as a function of a) T_G with $r_H = 50\%$, b) r_H for $T_G = 550°C$.

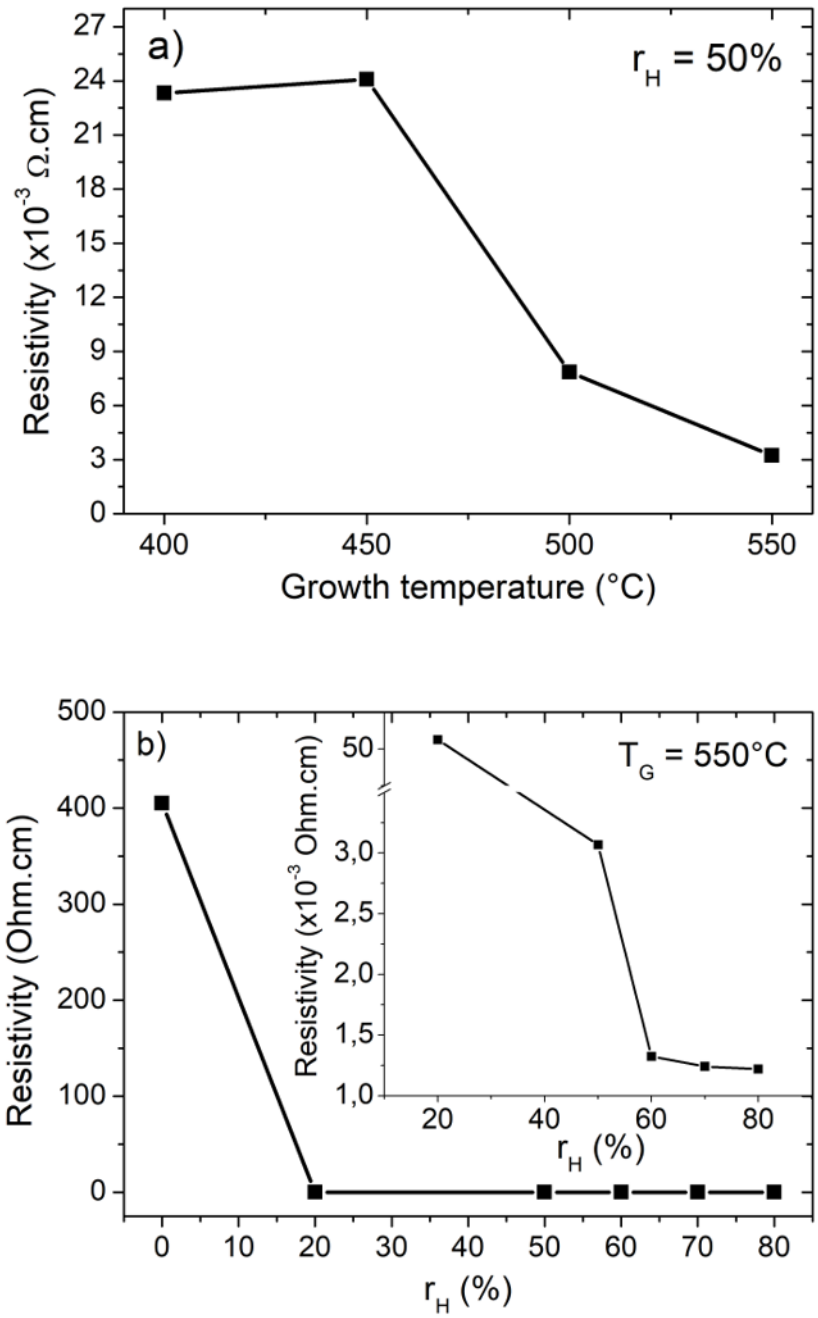

Figure 6: Electrical resistivities at room temperature obtained by the 4 probe method. a) for different values of T_G with $r_H = 50\%$, b) for different values of r_H with $T_G = 550°C$.

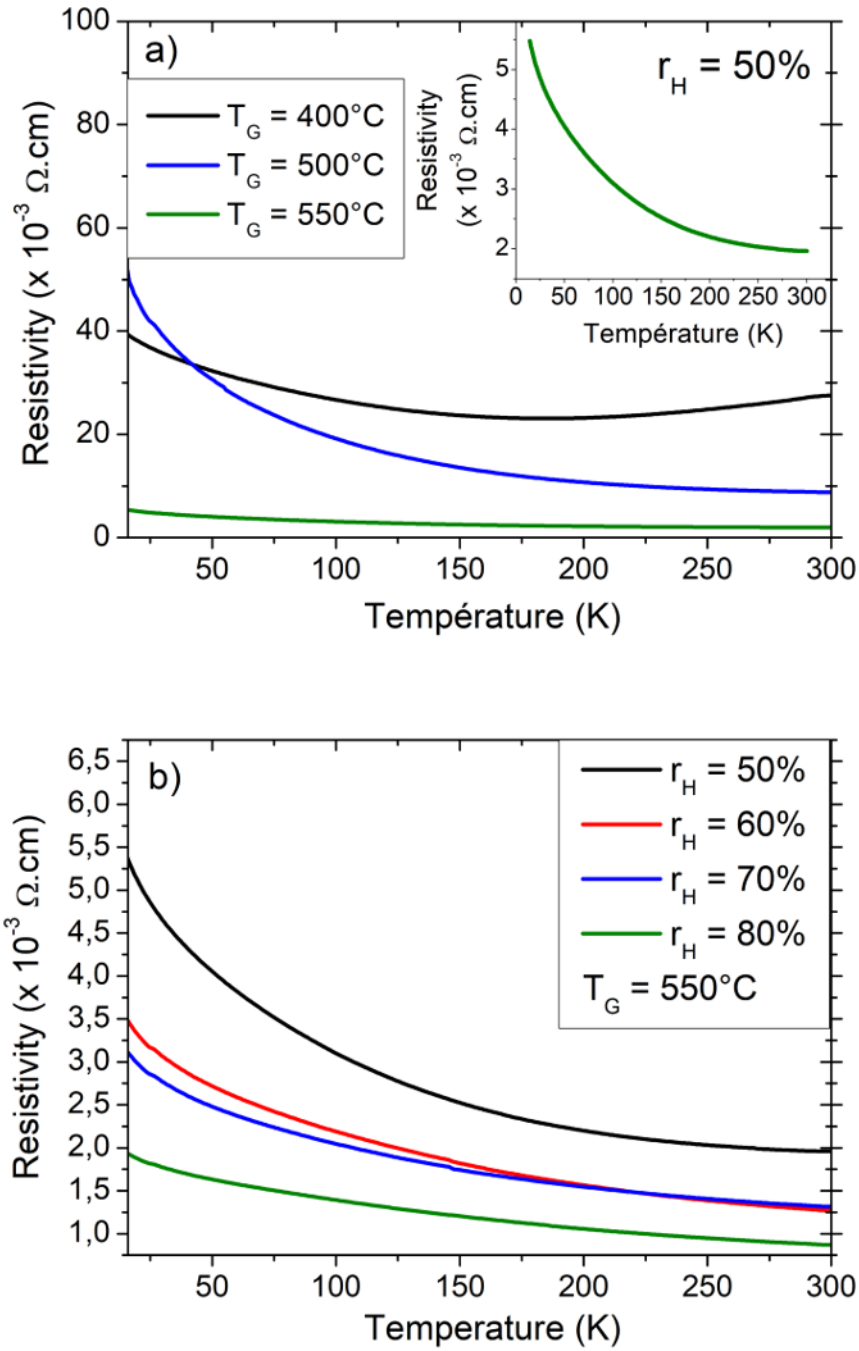

Figure 7: Electrical resistivities as a function of the temperature, a) for different values of T_G with $r_H = 50\%$, b) for different values of r_H with $T_G = 550°C$.

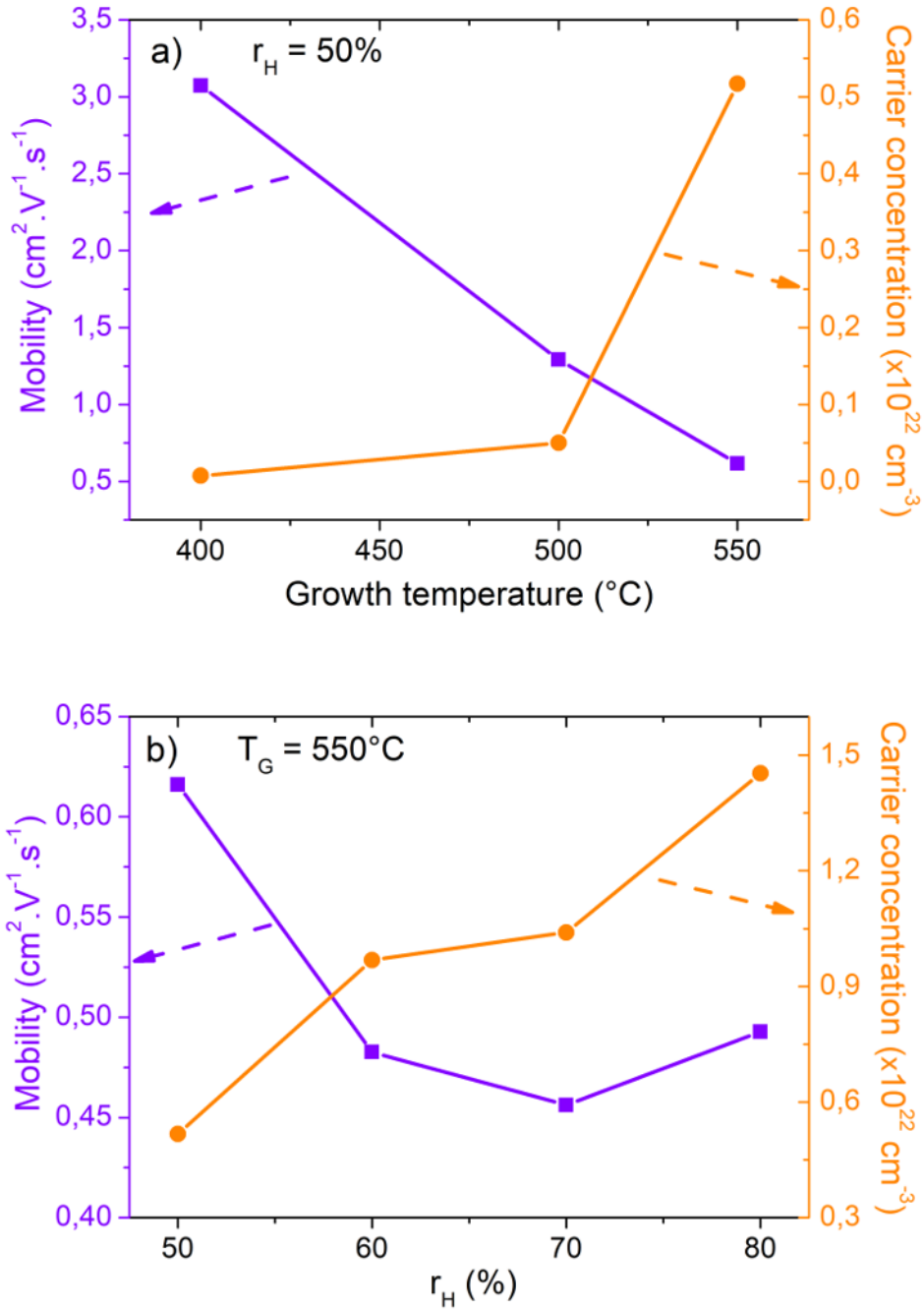

Figure 8: Transport properties at 300K. a) carrier concentration evolution at room temperature for different values of T_G and r_H, b) carrier mobility at room temperature for different values T_G and r_H

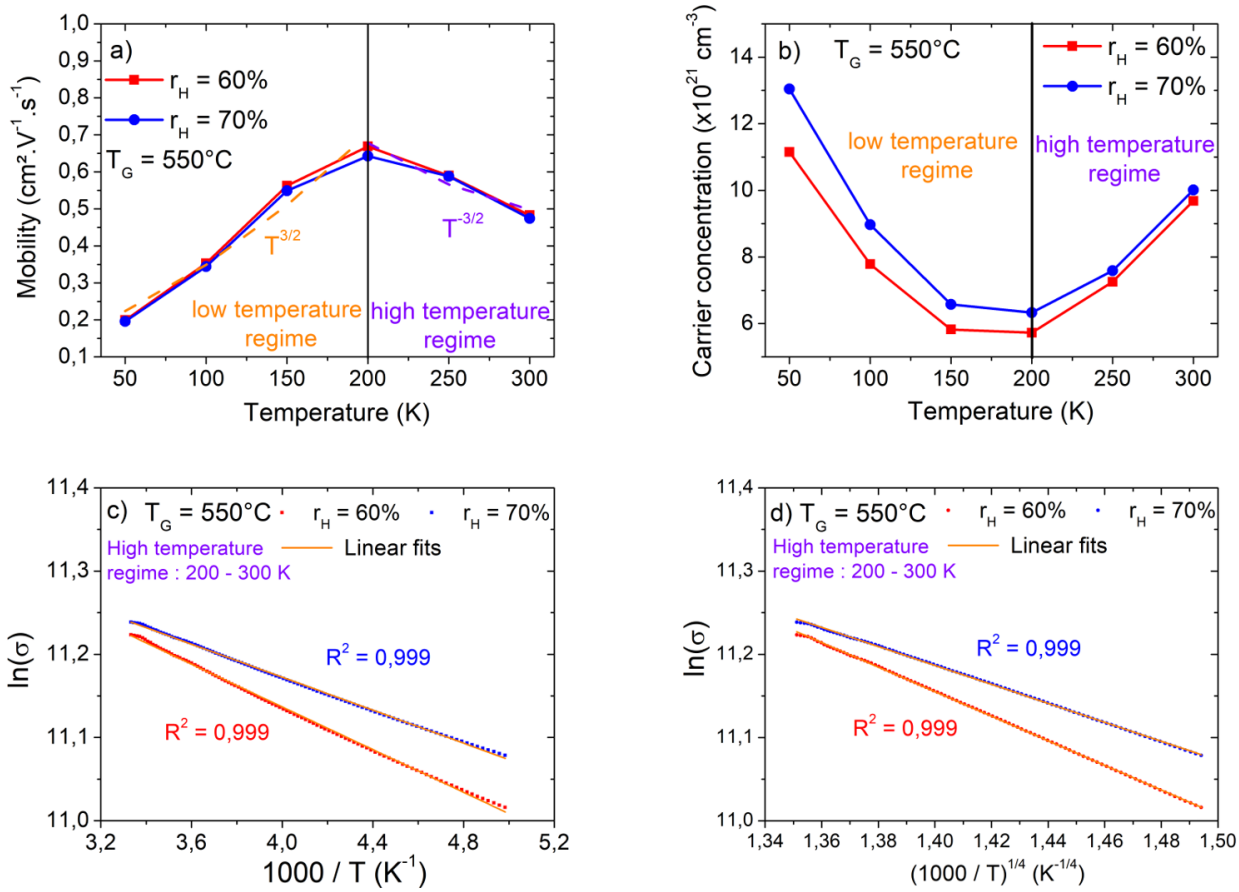

Figure 9: a) carrier mobility as a function of temperature for different values of r_H and T_G = 550°C, b) carrier concentration as a function of temperature for different values of r_H and T_G = 550°C, c) Plot of ln(σ) as the function of 1000/T for T between 200 and 300 K and for different values of r_H and T_G = 550°C, d) Plot of ln(σ) as the function of $(1000/T)^{1/4}$ for T between 200 and 300 K and for different values of r_H and T_G = 550°C.

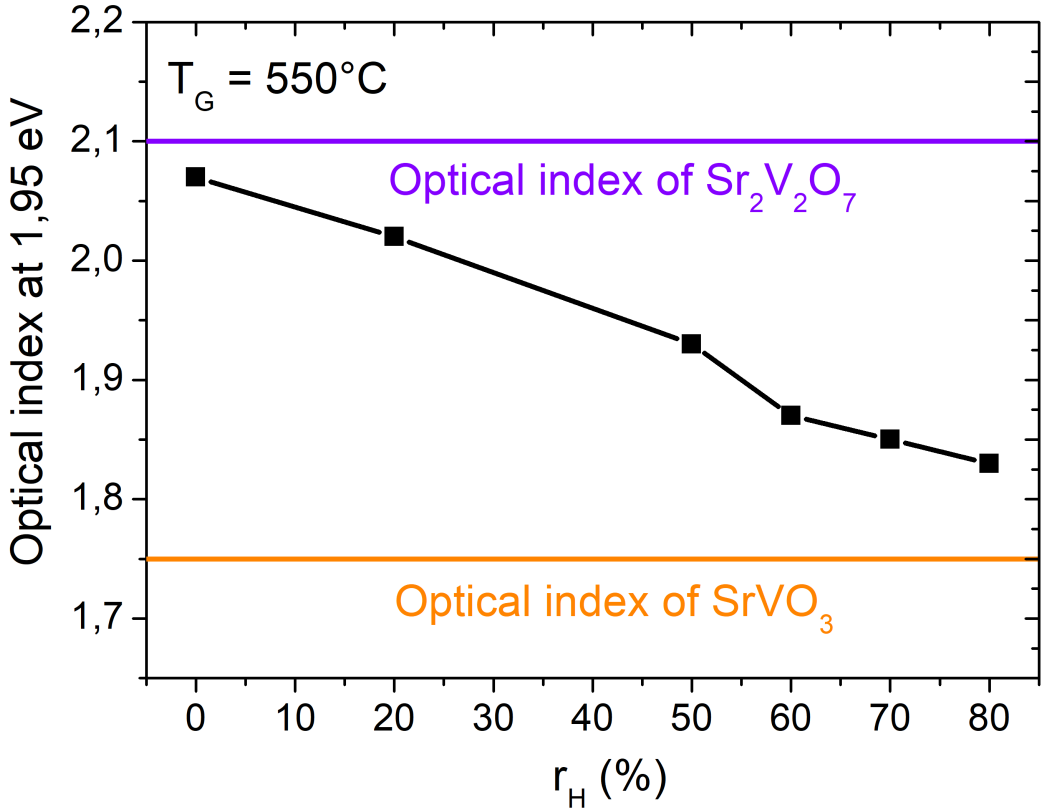

Figure 10: Evolution of the optical index for an incident photon energy of 1.95 eV as a function of r_H for $T_G = 550°C$.

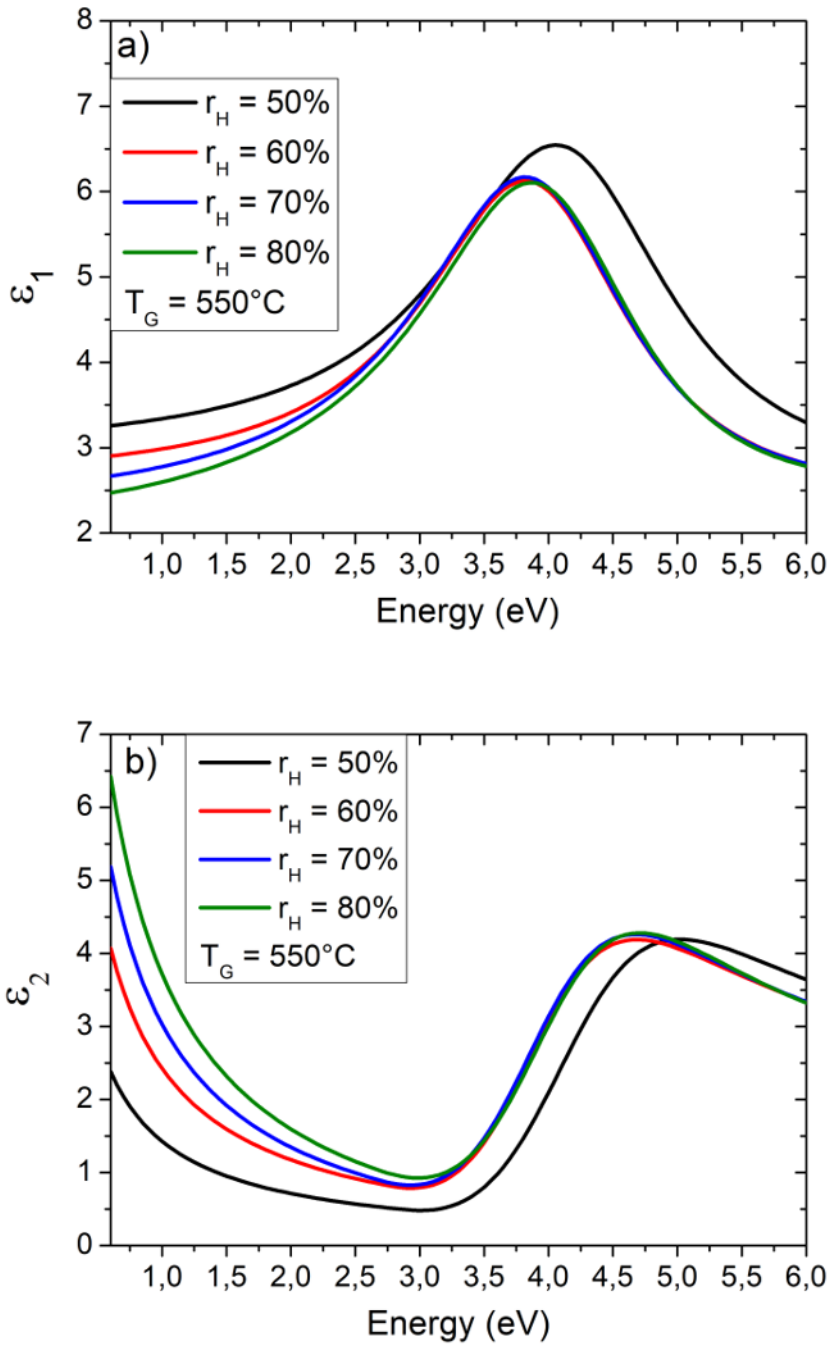

Figure 11: a) Evolution of the real part of the dielectric permittivity as a function of the energy for different values of r_H with $T_G = 550°C$, b) Evolution of the imaginary part of the dielectric permittivity as a function of the energy for different values of r_H with $T_G = 550°C$.

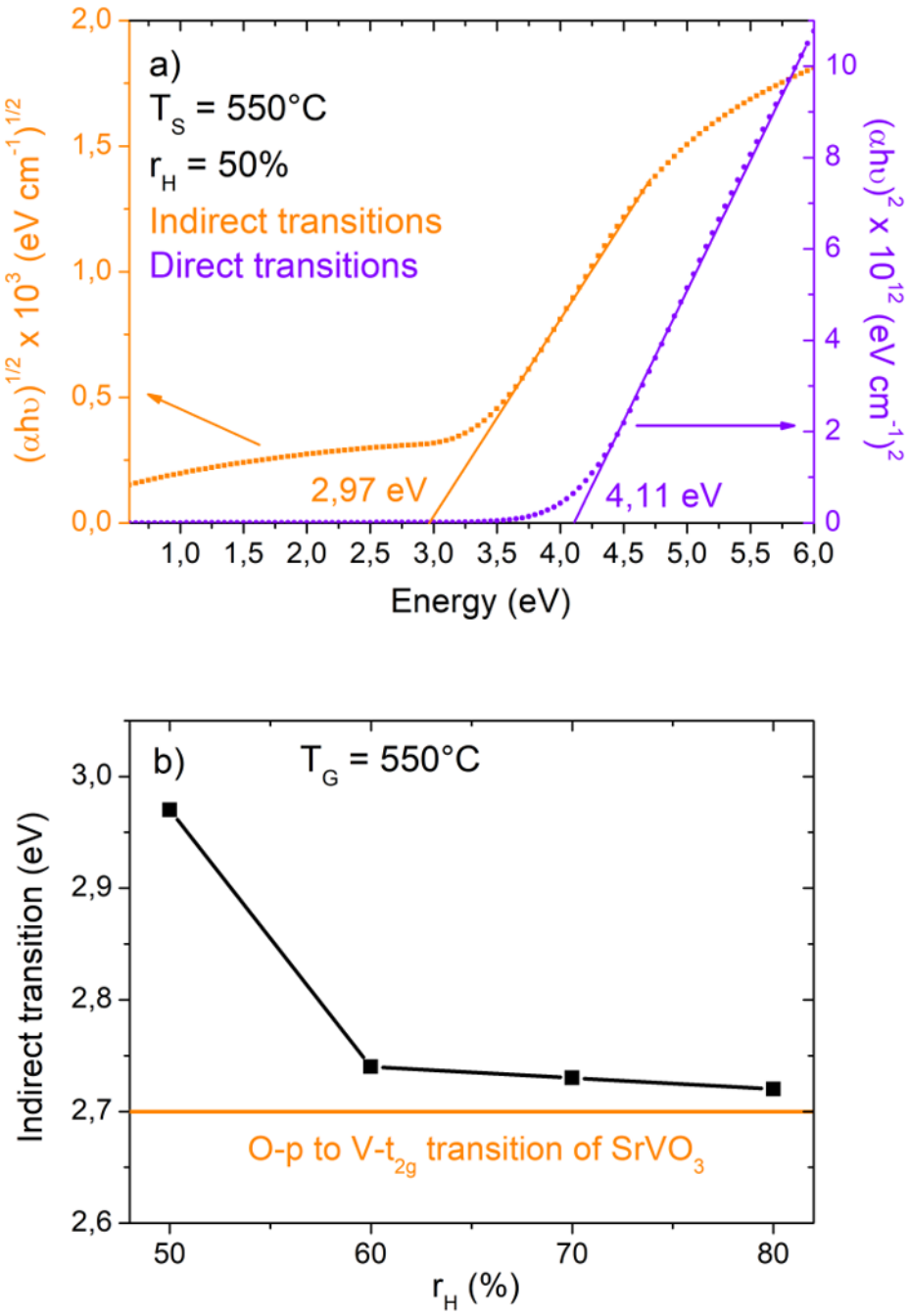

Figure 12: a) Tauc plots of SVO film grown at 550°C with 50% of hydrogen rate, plotted for direct (purple) and indirect (orange) optical transitions, b) Energy bandgap for an indirect transition as a function of r_H with T_G = 550°C.

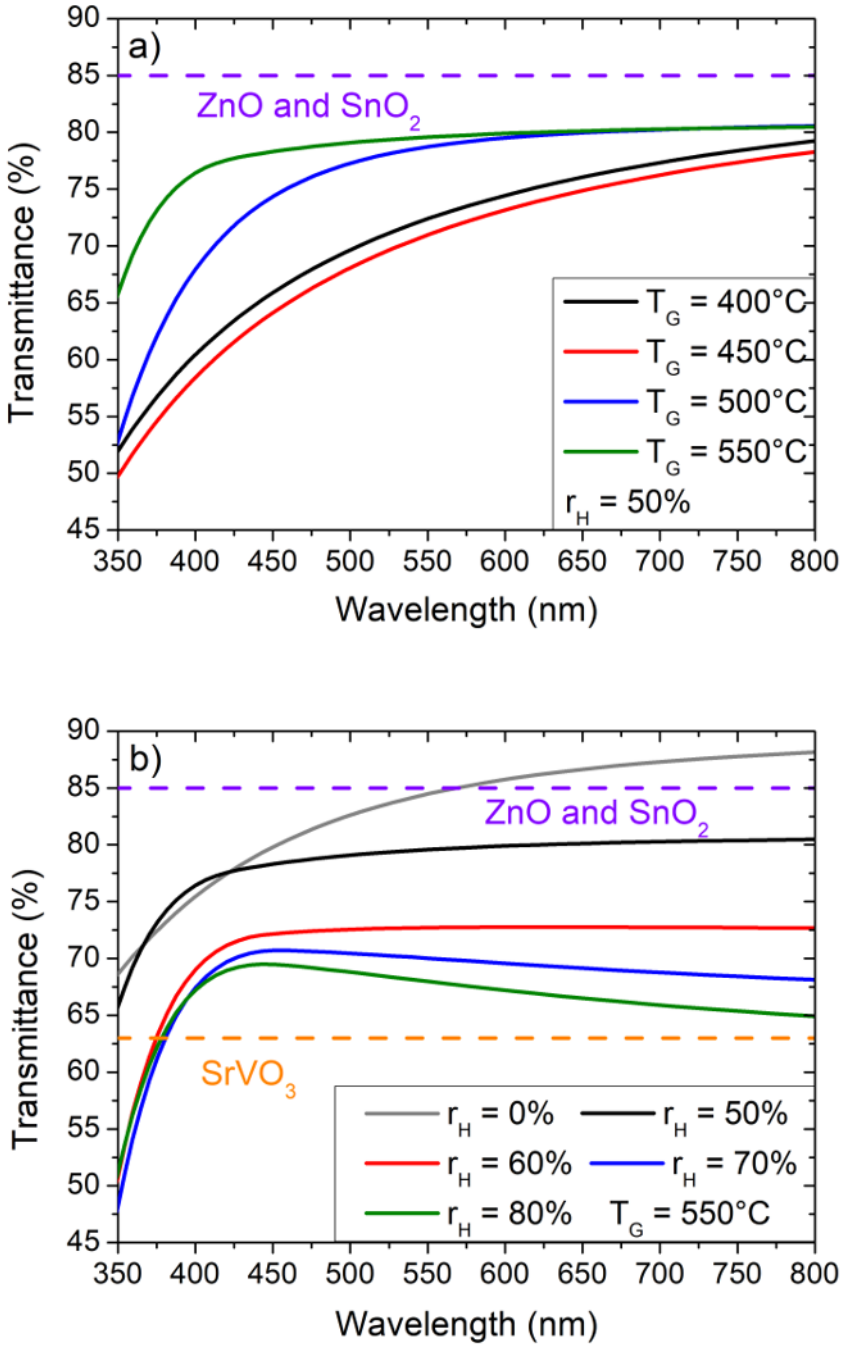

Figure 13: Evolution of transmittance as a function of the wavelengh for, a) different values of T_G with $r_H = 50\%$, b) different values of r_H with $T_G = 550°C$.

References

(1) Zhang, L.; Zhou, Y.; Guo, L.; Zhao, W.; Barnes, A.; Zhang, H.-T.; Eaton, C.; Zheng, y.; Brahlek, M.; Iqbal, H.; Podraza, N.; Chan, M.; Gopalan, V.; Rabe, K.; Engel-Herbert, R. Correlated metals as transparent conductors. *Nature materials* **2015**, *15*, 204–210.

(2) Boileau, A.; Cheikh, A.; Fouchet, A.; David, A.; Escobar-Galindo, R.; Labbe, C.; Marie, P.; Gourbilleau, F.; Lüders, U. Optical and electrical properties of the transparent conductor $SrVO_3$ without long-range crystalline order. *Applied Physics Letters* **2018**, *112*, 021905.

(3) Moyer, J.; Eaton, C.; Engel-Herbert, R. Highly Conductive $SrVO_3$ as a Bottom Electrode for Functional Perovskite Oxides. *Advanced materials (Deerfield Beach, Fla.)* **2013**, *25*, 3578–3582.

(4) Boileau, A.; Cheikh, A.; Fouchet, A.; David, A.; Labbe, C.; Marie, P.; Gourbilleau, F.; Lüders, U. Tuning of the Optical Properties of the Transparent Conducting Oxide $SrVO_3$ by Electronic Correlations. *Advanced Optical Materials* **2019**, *7*, 1801516.

(5) Berini, B.; Demange, V.; Bouttemy, M.; Popova, E.; Keller, N.; Dumont, Y.; Fouchet, A. Control of High Quality $SrVO_3$ Electrode in Oxidizing Atmosphere. *Advanced Materials Interfaces* **2016**, *3*, 1600274.

(6) Mirjolet, M.; Vasili, H.; López-Conesa, L.; Estradé, S.; Peiró, F.; Santiso, J.; Sanchez, F.; Machado, P.; Gargiani, P.; Valvidares, S.; Fontcuberta, J. Independent Tuning of Optical Transparency Window and Electrical Properties of Epitaxial $SrVO_3$ Thin Films by Substrate Mismatch. *Advanced Functional Materials* **2019**, *29*, 1904238.

(7) Mirjolet, M.; Rivadulla, F.; Marsik, P.; Borisov, V.; Valentí, R.; Fontcuberta, J. Electron–Phonon Coupling and Electron–Phonon Scattering in $SrVO_3$. *Advanced Science* **2021**, *8*, 200407.

(8) Mirjolet, M.; Kataja, M.; Hakala, T.; Komissinskiy, P.; Alff, L.; Herranz, G.; Fontcuberta, J. Optical Plasmon Excitation in Transparent Conducting $SrNbO_3$ and $SrVO_3$ Thin Films. *Advanced Optical Materials* **2021**, *9*, 2100520.

(9) Mirjolet, M.; Vasili, H. B.; Valadkhani, A.; Santiso, J.; Borisov, V.; Gargiani, P.; Valvidares, M.; Valentí, R.; Fontcuberta, J. Orbital occupancy and hybridization in strained $SrVO_3$ epitaxial films. *Phys. Rev. Mater.* **2021**, *5*, 095002.

(10) Mirjolet, M.; Sánchez, F.; Fontcuberta, J. High Carrier Mobility, Electrical Conductivity, and Optical Transmittance in Epitaxial $SrVO_3$ Thin Films. *Advanced Functional Materials* **2019**, *29*, 1808432.

(11) Moon, B.; Ishiwara, H. Epitaxial growth of conductive strontium-vanadate films on Si(100) substrates and their electrical resistivities. *Journal of Crystal Growth - J Cryst Growth* **1996**, *162*, 154–160.

(12) Gu, M.; Wolf, S.; Lu, J. Two-Dimensional Mott Insulators in $SrVO_3$ Ultrathin Films. *Advanced Materials Interfaces* **2014**, *1*, 1300126.

(13) Jung, D. H.; So, H. S.; Lee, H. Structural and electrical properties of transparent conductor $SrVO_3$ thin films grown using radio frequency sputtering deposition. *Journal of Vacuum Science and Technology A: Vacuum, Surfaces and Films* **2019**, *37*, 021507.

(14) Sharma, A.; Varshney, M.; Lim, W.; Shin, H.-J.; Singh, J.; Won, S. O.; Chae, K. Mechanistic insights on electronic properties and electronic/atomic structure aspects in orthorhombic $SrVO_3$ thin films: XANES-EXAFS study. *Phys. Chem. Chem. Phys.* **2017**, *19*, 6397–6405.

(15) Marks, S. D.; Lin, L.; Zuo, P.; Strohbeen, P. J.; Jacobs, R.; Du, D.; Waldvogel, J. R.; Liu, R.; Savage, D. E.; Booske, J. H.; Kawasaki, J. K.; Babcock, S. E.; Morgan, D.; Evans, P. G. Solid-phase epitaxial growth of the correlated-electron transparent conducting oxide $SrVO_3$. *Phys. Rev. Mater.* **2021**, *5*, 083402.

(16) Boileau, A.; Cibert, C.; David, A.; Fouchet, A.; Gourbilleau, F.; Labbé, C.; Lüders, U.; Poullain, G. Buffer layer for the crystal growth of metal oxides of perovskite type in particular on amorphous substrates. *FR3113185* **2022**,

(17) Rath, M.; Mezhoud, M.; El Khaloufi, O.; Lebedev, O.; Cardin, J.; Labbé, C.; Gourbilleau, F.; Polewczyk, V.; Vinai, G.; Torelli, P.; Fouchet, A.; David, A.; Prellier, W.; Lüders, U. Artificial Aging of Thin Films of the Indium-Free Transparent Conducting Oxide SrVO 3. *ACS Applied Materials & Interfaces* **2023**, *15*, 20240–20251.

(18) Jolivet, A.; Labbé, C.; Frilay, C.; Debieu, O.; Marie, P.; Horcholle, B.; Lemarié, F.; Portier, X.; Grygiel, C.; Duprey, S.; Jadwisienczak, W.; Ingram, D.; Upadhyay, M.; David, A.; Fouchet, A.; Lüders, U.; Cardin, J. Structural, optical, and electrical properties of TiO_2 thin films deposited by ALD: Impact of the substrate, the deposited thickness and the deposition temperature. *Applied Surface Science* **2023**, *608*, 155214.

(19) Gourbilleau, F.; Portier, X.; Ternon, C.; Voivenel, P.; Madelon, R.; Rizk, R. Si-rich/SiO_2 nanostructured multilayers by reactive magnetron sputtering. *Applied Physics Letters* **2001**, *78*, 3058–3060.

(20) Ternon, C.; Gourbilleau, F.; Portier, X.; Voivenel, P.; Dufour, C. An original approach for the fabrication of Si/SiO_2 multilayers using reactive magnetron sputtering. *Thin Solid Films* **2002**, *419*, 5–10.

(21) Luo, E.; Heun, S.; Wollschläger, J.; Henzler, M. Surface roughness and conductivity of thin Ag films. *Physical review. B, Condensed matter* **1994**, *49*, 4858–4865.

(22) Timoshevskii, V.; Ke, Y.; Guo, H.; Gall, D. The influence of surface roughness on electrical conductance of thin Cu films: An ab initio study. *Journal of Applied Physics* **2008**, *103*, 113705 – 113705.

(23) Ketenoglu, D.; Ünal, B. Influence of surface roughness on the electrical conductivity of

semiconducting thin films. *Physica A: Statistical Mechanics and its Applications* **2013**, *392*, 3008–3017.

(24) Inoue, I.; Goto, O.; Makino, H.; Hussey, N.; Ishikawa, M. Band-width control in a perovskite-type $3d^1$ correlated metal $Ca_{1-x}Sr_xVO_3$. I. Evolution of the electronic properties and effective mass. *Physical Review B* **1998**, *58*, 4372.

(25) Varignon, J.; Bibes, M.; Zunger, A. Origin of band gaps in 3d perovskite oxides. *Nature Communications* **2019**, *10*, 1658.

(26) Lai, L.-W.; Lee, C.-T. Investigation of optical and electrical properties of ZnO thin films. *Materials Chemistry and Physics* **2008**, *110*, 393–396.

(27) Lu, Y.; Hwang, W.-S.; Liu, W.; Yang, J.-R. Effect of RF power on optical and electrical properties of ZnO thin film by magnetron sputtering. *Materials Chemistry and Physics* **2001**, *72*, 269–272.

(28) Cho, S.-H. Effects of Growth Temperature on the Properties of ZnO Thin Films Grown by Radio-frequency Magnetron Sputtering. *Transactions on Electrical and Electronic Materials* **2009**, *10*, 185–188.

(29) Brousseau, J.-L.; Bourque, H.; Tessier, A.; Leblanc, R. Electrical properties and topography of SnO_2 thin films prepared by reactive sputtering. *Applied Surface Science* **1997**, *108*, 351–358.

(30) Kim, H.-R.; Lee, G.-H.; Kim, J. H. Effects of hydrogen plasma treatment on the structural and electrical properties of sputter-deposited SnO_2 thin films. *Journal of Physics D: Applied Physics* **2011**, *44*, 185203.

(31) Kim, S.; Oliver, M. Structural, electrical, and optical properties of reactively sputtered SnO_2 thin films. *Metals and Materials International - MET MATER INT* **2010**, *16*, 441–446.

(32) Kim, Y.; Lee, W.; Jung, D.-R.; Kim, J.; Nam, S.; Kim, H.; Park, B. Optical and electronic properties of post-annealed ZnO:Al thin films. *Applied Physics Letters* **2010**, *96*, 171902.

(33) Youssef, A.; Abderrazak, L.; Hartiti, B.; Ridah, A.; Thevenin, P.; Siadat, M. Structural, optical and electrical properties of ZnO:Al thin films for optoelectronic applications. *Optical and Quantum Electronics* **2014**, *46*, 229–234.

(34) Lennon, C.; Tapia, R.; Kodama, R.; Chang, Y.; Sivananthan, s.; Deshpande, M. Effects of Annealing in a Partially Reducing Atmosphere on Sputtered Al-Doped ZnO Thin Films. *Journal of Electronic Materials* **2009**, *38*, 1568–1573.

(35) Conwell, E.; Weisskopf, V. F. Theory of Impurity Scattering in Semiconductors. *Phys. Rev.* **1950**, *77*, 388–390.

(36) Chattopadhyay, D.; Queisser, H. J. Electron scattering by ionized impurities in semiconductors. *Rev. Mod. Phys.* **1981**, *53*, 745–768.

(37) Tang, L.; Long, M.-Q.; Wang, D.; Shuai, Z. The role of acoustic phonon scattering in charge transport in organic semiconductors: A first-principles deformation-potential study. *Science in China Series B Chemistry* **2009**, *52*, 1646–1652.

(38) Bardeen, J.; Shockley, W. Deformation Potentials and Mobilities in Non-Polar Crystals. *Phys. Rev.* **1950**, *80*, 72–80.

(39) Seitz, F. On the Mobility of Electrons in Pure Non-Polar Insulators. *Phys. Rev.* **1948**, *73*, 549–564.

(40) Kunets, V. P.; Prosandeev, S.; Mazur, Y. I.; Ware, M. E.; Teodoro, M. D.; Dorogan, V. G.; Lytvyn, P. M.; Salamo, G. J. Isotropic Hall effect and "freeze-in" of carriers in the InGaAs self-assembled quantum wires. *Journal of Applied Physics* **2011**, *110*, 083714.

(41) Bierwagen, O.; Speck, J. S. High electron mobility In_2O_3(001) and (111) thin films with non degenerate electron concentration. *Applied Physics Letters* **2010**, *97*, 072103.

(42) Makise, K.; Shinozaki, B.; Asano, T.; Yano, K.; Nakamura, H. Activation like behaviour on the temperature dependence of the carrier density in In_2O_3-ZnO films. *Journal of Physics: Conference Series* **2012**, *400*, 042043.

(43) Mao, J.; Wu, Y.; Song, S.; Shuai, J.; Liu, Z.; Pei, Y.; Ren, Z. Anomalous electrical conductivity of n-type Te-doped $Mg_{3.2}Sb_{1.5}Bi_{0.5}$. *Materials Today Physics* **2017**, *3*, 1–6.

(44) Weller, P. F. An introduction to principles of the solid state. Extrinsic semiconductors. *Journal of Chemical Education* **1971**, *48*, 831.

(45) Chanda, S.; Saha, S.; Dutta, A.; Krishna Murthy, J.; Venimadhav, A.; Shannigrahi, S.; Sinha, T. P. Magnetic ordering and conduction mechanism of different electroactive regions in Lu_2NiMnO_6. *Journal of Applied Physics* **2016**, *120*, 134102.

(46) Hill, R. M. Variable-range hopping. *physica status solidi (a)* **1976**, *34*, 601–613.

(47) Rosenbaum, R. Crossover from Mott to Efros-Shklovskii variable-range-hopping conductivity in In_xO_y films. *Phys. Rev. B* **1991**, *44*, 3599–3603.

(48) Rudra, M.; Tripathi, H.; Dutta, A.; Sinha, T. Existence of nearest-neighbor and variable range hopping in Pr_2ZnMnO_6 oxygen-intercalated pseudocapacitor electrode. *Materials Chemistry and Physics* **2021**, *258*, 123907.

(49) Schira, R.; Latouche, C. DFT and Hybrid-DFT calculations on the electronicproperties of vanadate materials: theory meets experiments. *New Journal of Chemistry* **2020**, *44*, 11602–11607.

(50) Roth, J.; Kuznetsova, T.; Miao, L.; Pogrebnyakov, A.; Alem, N.; Engel-Herbert, R.

Self-regulated growth of [111]-oriented perovskite oxide films using hybrid molecular beam epitaxy. *APL Materials* **2021**, *9*, 021114.

(51) Boileau, A.; Hurand, S.; Baudouin, F.; Lüders, U.; Dallocchio, M.; Berini, B.; Cheikh, A.; David, A.; Paumier, F.; Girardeau, T.; Marie, P.; Labbe, C.; Cardin, J.; Aureau, D.; Frégnaux, M.; Guilloux-Viry, M.; Prellier, W.; Dumont, Y.; Demange, V.; Fouchet, A. Highly Transparent and Conductive Indium-Free Vanadates Crystallized at Reduced Temperature on Glass Using a 2D Transparent Nanosheet Seed Layer. *Advanced Functional Materials* **2021**, *32*, 2108047.

(52) Tauc, J. Optical Properties and Electronic Structure of Amorphous Semiconductors. *Springer US* **1969**, 123–136.

(53) Ghobadi, N. Band gap determination using absorption spectrum fitting procedure. *International Nano Letters* **2013**, *3*, 2.

(54) Mohammadi, M.; Xie, R.; Hadaeghi, N.; Radetinac, A.; Arzumanov, A.; Komissinskiy, P.; Zhang, H.; Alff, L. Tailoring Optical Properties in Transparent Highly Conducting Perovskites by Cationic Substitution. *Advanced Materials* **2023**, *35*, 2206605.

(55) Gu, X.-j.; Luo, Z.-l.; Dong, Y.-q.; Zhou, J.-t.; Xu, H.; Hong, B.; Gao, C. Redox controllable switch of crystalline phase and physical property in $SrVO_x$ epitaxial films. *Chinese Journal of Chemical Physics* **2019**, *32*, 727–730.
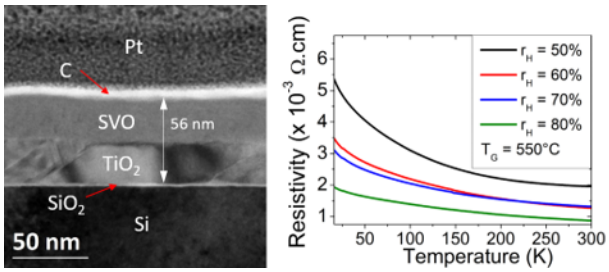
For Table of Contents Use Only